Retraction

Retracted: Marine Underwater Landscape Image Design Based on Bright Color Compensation and GAN Model Generation

Journal of Sensors

This article has been retracted by Hindawi following an investigation undertaken by the publisher [1]. This investigation has uncovered evidence of one or more of the following indicators of systematic manipulation of the publication process:

(1) Discrepancies in scope

(2) Discrepancies in the description of the research reported

(3) Discrepancies between the availability of data and the research described

(4) Inappropriate citations

(5) Incoherent, meaningless and/or irrelevant content included in the article

(6) Manipulated or compromised peer review

The presence of these indicators undermines our confidence in the integrity of the article's content and we cannot, therefore, vouch for its reliability. Please note that this notice is intended solely to alert readers that the content of this article is unreliable. We have not investigated whether authors were aware of or involved in the systematic manipulation of the publication process.

Wiley and Hindawi regrets that the usual quality checks did not identify these issues before publication and have since put additional measures in place to safeguard research integrity.

We wish to credit our own Research Integrity and Research Publishing teams and anonymous and named external researchers and research integrity experts for contributing to this investigation.

The corresponding author, as the representative of all authors, has been given the opportunity to register their agreement or disagreement to this retraction. We have kept a record of any response received.

References

[1] J. Yuan, L. Zhang, and C. Kim, "Marine Underwater Landscape Image Design Based on Bright Color Compensation and GAN Model Generation," *Journal of Sensors*, vol. 2023, Article ID 1976819, 10 pages, 2023.

Research Article

Marine Underwater Landscape Image Design Based on Bright Color Compensation and GAN Model Generation

Jingwen Yuan,[1] Longlong Zhang,[1] and ChulSoo Kim [2]

[1]*Design Engineering, Department of Marine Design Convergence Engineering, Pukyong National University, Busan 612022, Republic of Korea*
[2]*Department of Industrial Design, Pukyong National University, Busan 612022, Republic of Korea*

Correspondence should be addressed to ChulSoo Kim; bosen@pukyong.ac.kr

Traditional denoising algorithms cannot effectively deal with these images with different blurriness and color deviation. Especially for underwater operations, the images are not clear, which makes it difficult for operators to act as agents. To solve this problem, this paper proposes a bright color compensation and fusion method. Underwater image enhancement algorithm uses generated countermeasure network (GAN). First, the original image is color compensated using the bright channel to obtain a color-compensated image; then, adaptive contrast stretching is performed on the color-compensated image to obtain a clear image with high contrast. It can be seen from the experiment that the PSNR of the marine landscape map can reach 21.9329, and the SSIM can reach 0.7329, which can provide useful help for the field of underwater image enhancement.

1. Introduction

Underwater images are widely used in marine environment, industry, and military fields, but due to the effects. The degraded quality of underwater images often affects the accuracy of the application when used for underwater image recognition and understanding [1]. With the decrease of available resources on land, the development and utilization of marine resources has become an urgent issue for human beings. In recent years, underwater robots have been widely used in marine resource exploration and other areas. Due to the complex underwater environment, the images captured by underwater robots are often severely degraded, mainly in the form of blur, low contrast, color deviation, etc. [2, 3]. Underwater enhancement methods include bright channel color compensation and fusion and multiscale Retinex. These methods use objective measures to enhance the quality of underwater images without considering the physical process of underwater imaging and are not suitable for underwater imaging with different physical characteristics and may lead to more obvious noise in the enhancement

process [4]. However, because the attenuation coefficients of different wavelengths of light underwater are different, the DCP algorithm cannot achieve the expected results when applied directly to underwater image recovery. Underwater enhancement methods include bright channel color compensation and fusion and multiscale Retinex. These methods use objective measures to enhance the quality of underwater images without considering the physical process of underwater imaging, which is not suitable for underwater imaging with different physical characteristics and may lead to more pronounced noise in the enhancement process [5, 6]. The underwater image recovery method relies on the underwater imaging model and considers the influence of the water body optical parameters, camera parameters, water body point expansion function, and scene distance on the underwater imaging and finally obtains a clear underwater image by the inverse solution [7].

The nonphysical model-based methods achieve image enhancement by adjusting the image pixel values to enhance visual perception. In recent years, the pyramid attention mechanism has been successfully applied in the field of semantic segmentation [8, 9], where the combination of

pyramid structure and attention mechanism can capture richer high-level features and better learn image details, thus effectively improving the performance of the model [10–13].

This paper proposes a bright color compensation and fusion. Underwater image enhancement algorithm is using generative adversarial networks (GAN). Use the bright channel to perform color compensation on the original image to obtain a color-compensated image; perform adaptive contrast stretching on the color-compensated image to obtain a clear image with high contrast.

2. Related Work

Underwater images are widely used in the marine environment, industry, and military fields, but they generally suffer from poor clarity, low contrast, and severe noise due to the effects of underwater light absorption, scattering, and suspended particles [14]. Literature [15] used image blurring and light absorption to estimate the transmittance map and improved the estimation of background light to optimize the recovery effect. However, most of these underwater recovery methods only consider the estimation of transmittance map and background light, ignoring the influence of a large amount of noise and edges in the underwater image on the recovery results [16, 17], so it may aggravate the noise of the image and even destroy the original edge information of the image [18, 19].

For example, in [20–23], a wavelength-dependent compensation algorithm was combined with an image defogging algorithm to recover underwater images, which can effectively eliminate the blue-green hue of underwater images and the effect of artificial light sources. In [24], a full variational Retinex (TV-R) model based on the TV rule term was proposed. In [25], a new fractional-order variational framework method is proposed by changing the number of rule terms from integer order to fractional order while introducing nonlocal operators.

3. Algorithms in This Paper

3.1. Variational Recovery Model Based on Laplace Operator. The underwater optical imaging model under natural illumination conditions can be expressed as

$$I(x, y) = t(x, y) \times J(x, y) + [1 - t(x, y) \times B], \quad (1)$$

where $I(x, y)$ is the acquired underwater image; $t(x, y)$ is the transmittance map of each channel; $J(x, y)$ is the undegraded underwater image; and B is the ambient background light. Based on the F-based variational model for foggy sky image recovery, Equation (1) is deformed: $s = \ln(B - J)$, $r = \ln(1/t)$, $1 = \ln(B - I)$. Based on the fact that light propagation in water has different attenuation ratios of red, blue, and green colors (red is the largest; blue and green are the second largest), which is different from the imaging process

of foggy sky images, we add a constraint term $|s - s_0|^2$ to adjust the color distortion of underwater images and thus establish the variational energy equation for underwater image recovery, namely,

$$E(s) = \operatorname{argmin}\left(a \int_\Omega |\Delta r| dx + \beta \int_\Omega |\Delta s| dx \right.$$
$$\left. + \frac{\mu}{2} \int_\Omega |r - r_0|^2 dx + \frac{\theta}{2} \int_\Omega |s - s_0|^2 dx + \frac{1}{2} |s - l - r|^2 dx \right), \quad (2)$$

$$s_0 = \ln\left[\frac{B - (s - c) \times (b - a)}{(d - c) + a}\right]. \quad (3)$$

3.2. Estimation of Background Light and Transmittance Map. The accuracy of the background light estimation can directly affect the results of underwater image recovery. The adaptive red channel a priori (ARC) algorithm considers the relationship between the attenuation coefficients of the three underwater channels, describes the high-intensity pixels of the underwater image in terms of saturation, and estimates the background light based on the green, blue, and inverted red channels, where the saturation and red channel estimation are defined as

$$J^{R-Sat}(x) = \min\left\{\min_{y \in \Omega(x)}\left[1 - J^R(y)\right], \min_{y \in \Omega(x)}\right.$$
$$\left. \cdot \left[J^G(y)\right], \min_{y \in \Omega(x)}\left[J^B(y)\right], \min_{y \in \Omega(x)}[\xi(y)]\right\} = 0. \quad (4)$$

To ensure the accuracy of the background light estimation, the red channel map of the original image I was calculated according to Equation (4) I^R. All the pixel values in the (I^R, I^G, I^B) 3-layer channel were sorted from the largest to smallest, and the coordinates of the points corresponding to the top 0.1% of the pixel values were calculated separately, and then, the corresponding pixel values were found in the 3 channels according to the coordinates of the points, and the average value of the calculated pixels in the region was used as the background light values of the different channels:

$$B_\lambda = \max_{x \in I}\left[\min_{y \in \Omega(x)} I_\lambda(y)\right], \lambda \in \{R, G, B\}. \quad (5)$$

Since the information loss occurs when solving the underwater image imaging model, the amount of information loss is inversely proportional to the transmittance t, and the attenuation coefficient of the red channel is the largest, so the loss of information can be reduced by estimating the red channel transmittance map a priori. Based on the red channel a priori, the transmittance map of the red channel is obtained as

$$t^R(x) = 1 - \min\left[\frac{\min_{y \in \Omega(x)}\left[1 - I^R(y)\right]}{1 - B_R}, \frac{\min_{y \in \Omega(x)}\left[I^G(y)\right]}{B_G}, \frac{\min_{y \in \Omega(x)}\left[I^B(y)\right]}{B_B}, \min_{y \in \Omega(x)}\xi(y)\right]. \quad (6)$$

The attenuation coefficient versus wavelength for the transmittance maps of different channels of underwater images can be expressed as

$$\frac{\beta^k}{\beta^R} = \frac{\beta^R\left(m\lambda^k + i\right)}{B^k\left(m\lambda^R + i\right)}, \quad k \in \{G, B\}. \tag{7}$$

Based on the ratio of the predicted transmittance map of the red channel and the attenuation coefficient, the transmittance maps of the green and blue channels were reestimated to obtain

$$t^k(x) = t^R(x)^{\beta^{\beta^k}/\beta^k}, \quad k \in \{G, B\}|^{\circ}. \tag{8}$$

Three underwater images are selected, and their respective red channel transmittance maps are derived by Equation (7), as shown in Figure 1, which shows the three degraded underwater images and the estimated red channel transmittance maps and the estimated background light values by the red channel a priori method.

3.3. ADMM Algorithm for Variational Recovery Model. The proposed variational model is solved numerically using the ADMM algorithm according to the iterative model of the Laplace term operator to improve its convergence speed:

(i) The auxiliary variables $p, v, \mathbf{w}$ are introduced and replaced by $\nabla r, \Delta r, \nabla s$, respectively, and assigned according to the ADMM solution method; the energy equation (2) is transformed into

$$
\begin{aligned}
E(r, s, p, v, \mathbf{w})^{\mathrm{T}} = \operatorname{argmin}\Bigg\{ & a\int_{\Omega}|v|dx + \beta\int_{\Omega}|w|dx \\
& + \frac{\mu}{2}\int_{\Omega}|r - r_0|^2 dx \int_{\Omega}\sigma_1|v - \nabla\mathbf{p}|dx \\
& + \frac{\mu_1}{2}\int_{\Omega}|v - \nabla\mathbf{p}|^2 dx + \int_{\Omega}\sigma_2|p - \nabla r|dx \\
& + \frac{\mu_2}{2}\int_{\Omega}|P - \nabla r|^2 dx + \int_{\Omega}\sigma_3|w - \nabla s|dx \\
& + \frac{\mu_3 + \theta}{2}\int_{\Omega}|s - s_0|^2 dx + \frac{1}{2}\int_{\Omega}|s - l - r|^2 dx \\
& + \int_{\Omega}|w - \nabla_s|^2 dx\Bigg\},
\end{aligned}
\tag{9}
$$

where α, β are nonnegative penalty parameters; $\sigma_1, \sigma_2, \sigma_3$ are Lagrangian multipliers.

(ii) Solve for $r, s, p, v, \mathbf{w}$

(1) Fix $s, p, v, \mathbf{w}$ to solve r. The Euler-Lagrange equation for r is

$$
\begin{aligned}
r_{i,j}^{k+1} &= \frac{s^k - l^k - \nabla\sigma_2^k - \mu_2\nabla\mathbf{p}^k + \mu_2 R^k + \mu r_0}{1 + 4\mu_2 + \mu}, \\
R^k &= r_{i+1,j}^k(x) + r_{i-1,j}^k(x) + r_{i,j+1}^k(x) + r_{i,j-1}^k(x) - 4r_{i,j}^k(x)
\end{aligned}
\tag{10}
$$

(2) Fixing $r, p, v, \mathbf{w}$ to solve for s, the Euler-Lagrange equation for s is

$$
\begin{aligned}
s^{k+1} &= \frac{\mu_5 S + r + l - \nabla\sigma_3^k - \mu_3\nabla w + \theta s_0}{1 + \theta + 4\mu_3}, \\
S &= s_{i+1,j}^k + s_{i-1,j}^k + s_{i,j+1}^k + s_{i,j-1}^k - 4s_{i,j}^k
\end{aligned}
\tag{11}
$$

(3) Fixing $r, s, v, \mathbf{w}$ and solving for p, the Euler-Lagrange equation for p is

$$
\begin{aligned}
p_1^{k+1} &= \frac{P_1 + \mu_2(\nabla_x) - \sigma_{21} - (\partial\sigma_1/\partial x) - \mu_1(\partial v/\partial x)}{2\mu_1 + \mu_2}, \\
p_2^{k+1} &= \frac{P_2 + \mu_2(\nabla r_y) - \sigma_{22} - (\partial\sigma_1/\partial y) - \mu_1(\partial v/\partial y)}{2\mu_1 + \mu_2}, \\
P_1 &= \mu_1\left(p_{1_{i+1,j}}^k + p_{2_{i-1,j}}^k\right) + \frac{\mu_1}{4}\left(p_{2_{i+1,j+1}}^k + p_{2_{i-1,j-1}}^k - p_{2_{i+1,j-1}}^k - p_{2_{i-1,j+1}}^k\right), \\
P_2 &= \mu_1\left(p_{2_{i,j+1}}^k + p_{2_{i,j-1}}^k\right) + \frac{\mu_1}{4}\left(p_{1_{i+1,j+1}}^k + p_{1_{i-1,j-1}}^k - p_{1_{i+1,j-1}}^k - p_{1_{i-1,j+1}}^k\right)
\end{aligned}
\tag{12}
$$

(4) Fixing $r, s, p, \mathbf{w}$ and solving for v. Using the generalized soft threshold formula for the variable v, the computer expression of the analytic solution is obtained as

$$v^{k+1} = \max\left(\left\|\nabla\mathbf{p}^k\right| - \frac{\sigma_1^k}{\mu_1}\right| - \frac{\alpha}{\mu}, 0\right)\frac{\nabla\mathbf{p}^k}{\left|\nabla\mathbf{p}^k\right|} \tag{13}$$

(5) Fix r, s, p, v to solve for $\mathbf{w}$, and use the generalized soft threshold formula to solve for the variable $\mathbf{w}$. The computer expression of the analytic solution is obtained as

$$w^{k+1} = \max\left(\left\|\nabla s^k\right| - \frac{\sigma_3^k}{\mu_3}\right| - \frac{\beta}{\mu_3}, 0\right)\frac{\nabla s^k}{\left|\nabla s^k\right|} \tag{14}$$

(iii) Update the Lagrangian multiplier $\sigma_1, \sigma_2, \sigma_3$
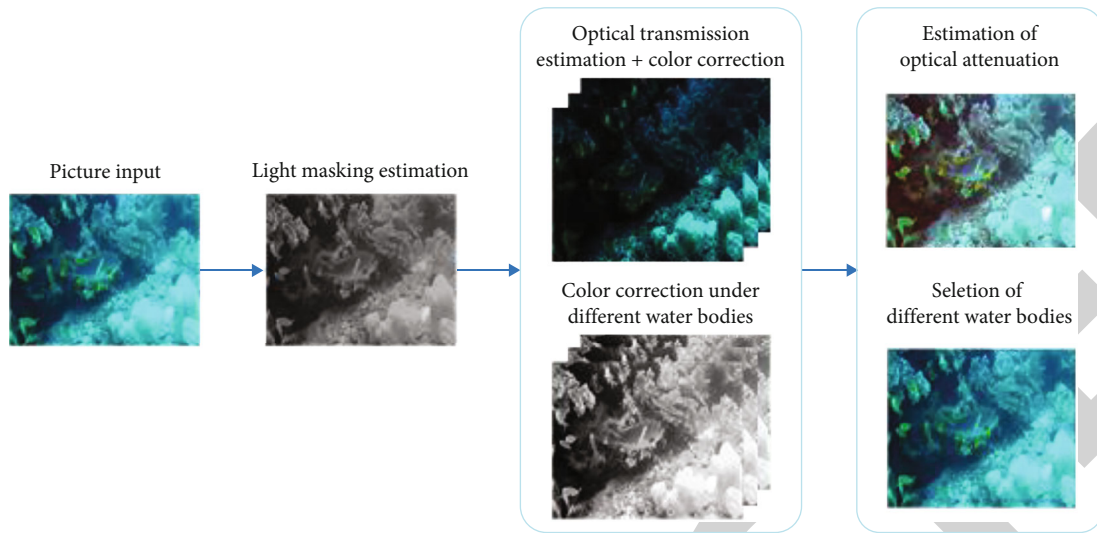
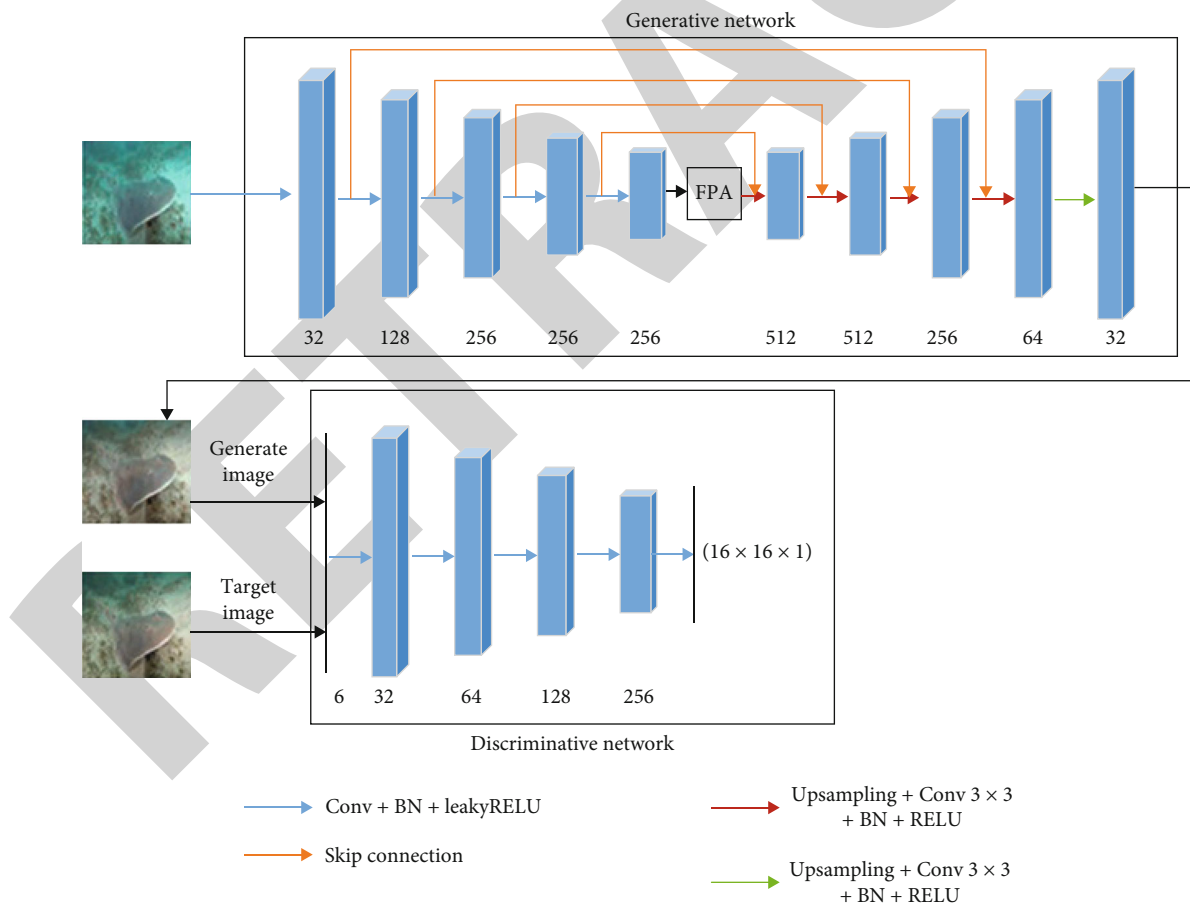FIGURE 1: Degraded underwater images and transmission maps.
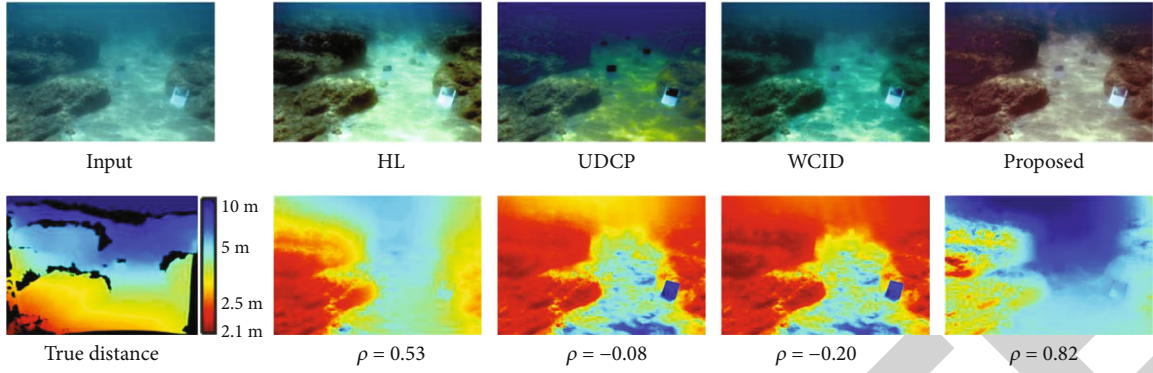

FIGURE 2: Structure of FPAGAN.

Figure 3: Results of comparative experiments without FPA module and with FPA module.

$$\begin{cases} \sigma_1^{k+1} = \sigma_1^k + \mu_1(v - \nabla \mathbf{p}), \\ \sigma_2^{k+1} = \sigma_2^k + \mu_2(\mathbf{p} - \nabla r), \\ \sigma_3^{k+1} = \sigma_3^k + \mu_3(\mathbf{w} + \nabla s) \end{cases} \tag{15}$$

Table 1: Experimental results on test set A.

Method	PSNR	SSIM
GAN	21.9329	0.7329
FPAGAN	22.3983	0.7417

Table 2: Experimental results on test set B.

Method	UIQM	IE	NIQE
GAN	2.9087	4.6886	42.5058
FPAGAN	2.9456	4.6953	37.6929

4. FPAGAN Enhancement Model

The algorithm takes paired underwater images as training data and constructs a multinomial loss function to enhance the output of the network model and finally obtains underwater images with improved contrast, vivid colors, and clarity by training the network model.

4.1. Model Structure. FPAGAN (generative adversarial network with feature pyramid attention) enhances degraded underwater images by using encoder and decoder to extract image features and combining them with feature pyramid attention module. The structure of FPAGAN is divided into two parts: the generative network and the discriminative network. The network structure and data processing flow of FPAGAN are shown in Figure 2.

4.2. Construction of the Loss Function. In this paper, the FPAGAN model is optimized by adversarial training of the generative network and the discriminative network, and the optimization process of the network corresponds to the optimization of the loss function. The loss function of the adversarial network is

$$L_{\text{adv}} = E(y)\{\log [D(y)]\} + E(x)\{\log \{1 - D[G(x)]\}\}, \tag{16}$$

where D denotes the discriminant network; G denotes the generative network; and E denotes the mathematical expectation.

During model training, the discriminant network is updated once, and then, the generator network is updated once to prevent the model gradient from disappearing. The model reaches dynamic equilibrium when the discriminant network cannot distinguish between the generated image and the reference image, and then, a clear underwater image is obtained. In order to reduce the human interference in the output image, three aspects are considered in this paper, namely, global similarity, image content, and color perception loss.

Global similarity loss: existing methods show that adding $L_1(L_2)$ loss to the objective function allows the generative network G to learn the global similarity between images. Since L_1 loss is not easy to introduce ambiguity, a L_1 loss term is added to the objective function:

$$L_1 = E_{x,y}\big[\|y - G(x)\|_1\big], \tag{17}$$

where x denotes the degraded underwater image; y denotes the reference image corresponding to the degraded image.

Color perception loss: this loss term facilitates G to generate enhanced images with similar color to the reference image, which is defined as follows:

$$\begin{aligned}
L_{\text{col}_p\text{er}} &= \sqrt{\frac{(512 + r_{\text{mean}})r^2}{256} + 4g^2 + \frac{(767 - r_{\text{mean}})b^2}{256}}, \\
r_{\text{mean}} &= \frac{y_{c\_r} + G(x)_{c\_r}}{2}, \\
r &= y_{c\_r} - G(x)_{c\_r}, \\
g &= y_{c\_g} - G(x)_{c\_g}, \\
b &= y_{c\_b} - G(x)_{c\_b},
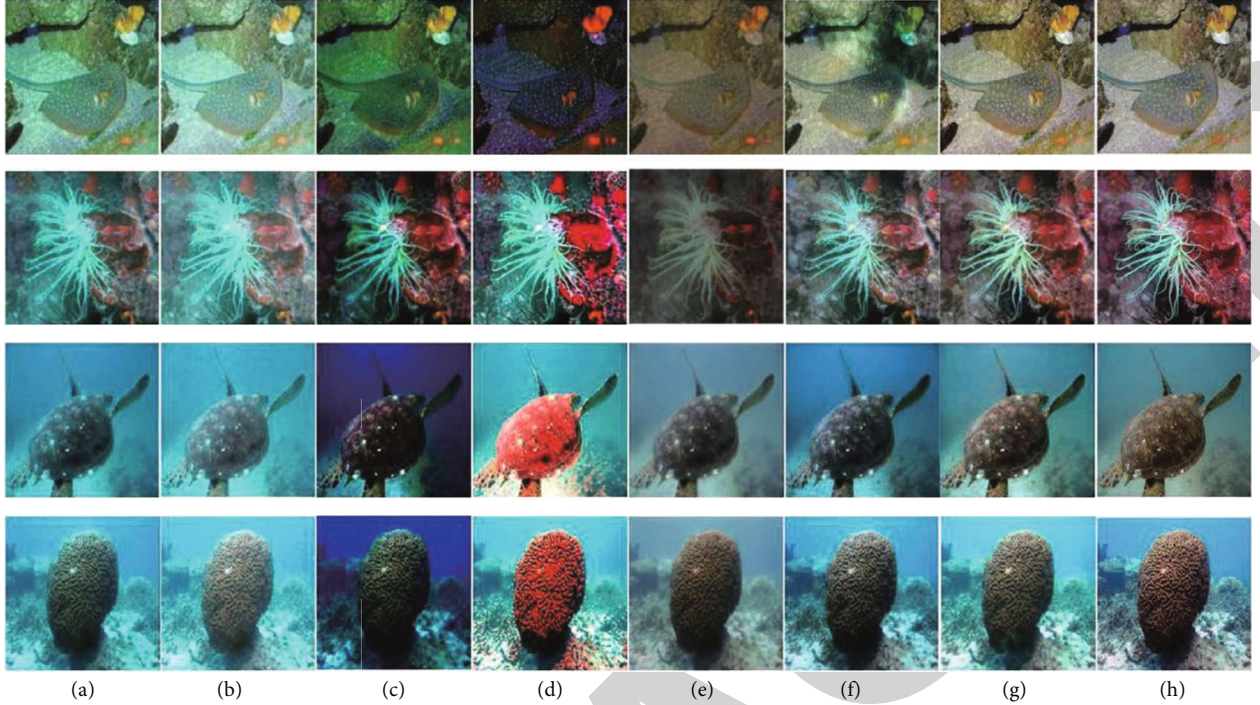\end{aligned} \tag{18}$$

(a)   (b)   (c)   (d)   (e)   (f)   (g)   (h)

FIGURE 4: Qualitative comparison of different methods on test set A. (a) Underwater images; (b) GC; (c) UDCP; (d)LDCP; (e) UWCNN; (f) FUnIE-GAN; (g) proposed method; (h) reference.

TABLE 3: Quantitative comparison on test set A.

Metrics	GC	UDCP	LDCP	UWCNN	FUnIE-GAN	Ours
PSNR	15.1829	13.2232	13.9796	16.1345	19.3573	22.3985
SSIM	0.6493	0.5355	0.5421	0.6062	0.6921	0.7418

where the subscripts c_r, c_g, c_b denote the red, green, and blue color channels of the image, respectively.

FPAGAN uses a multinomial loss function for network model learning, which facilitates the accelerated convergence of network parameters and improves the robustness of the model. The objective function is obtained by linearly superimposing the adversarial loss L_{adv}, L_1 loss function, content-aware loss L_{con}, and color-aware loss L_{col_per} to obtain

$$L = L_{adv} + \lambda_1 L_1 + \lambda_2 L_{con} + \lambda_3 L_{col\_per}, \tag{19}$$

where $\lambda_1, \lambda_2, \lambda_3$ represents the scaling factor, which is set to 0.6, 0.3, and 0.1, respectively, according to the experience.

5. Experimental Setup

The experiment is implemented under Windows OS, based on Tensorflow and Keras open source framework for deep learning. The computer configuration is as follows: NVIDIA GeForce RTX2070 Max-Q (8 GB) GPU, Inter Core i7-10750H CPU at 2.60 GHz, and 16 GB of RAM.

In this paper, the size of all training samples was reduced to $256 \times 256 \times 3$ and normalized to the interval [-1, 1]; the batch_size was 8; five different sizes of convolutional kernels were used in the network model, 7×7, 5×5, 4×4, 3×3, and 1×1, respectively; in addition, three different nonlinear activation functions were used to improve the generalization ability of the model. In addition, three different nonlinear activation functions are used to improve the generalization ability of the model.

5.1. Analysis and Discussion. The test set is divided into test set A and test set B. Test set A contains 46 underwater images with reference, and test set B contains 23 underwater images without reference. The validation set is generally used in the training process, and the enhancement effect can be verified on the validation set after each epoch, in order to find the problems of the model or parameters and verify the generalization ability of the model in time, so that we can make countermeasures in time. The test set is generally used after the training to evaluate the performance of the final trained model.

In order to verify the effectiveness of the algorithms in this paper, we compare them with existing underwater image enhancement methods, including nonphysical model-based methods (GC), physical model-based methods (UDCP, LDCP), and data-driven methods (UWCNN, FUnIE-GAN), through extensive experiments. In this paper, the effectiveness of the introduced FPA modules is firstly analyzed, and then, the experimental results of the above
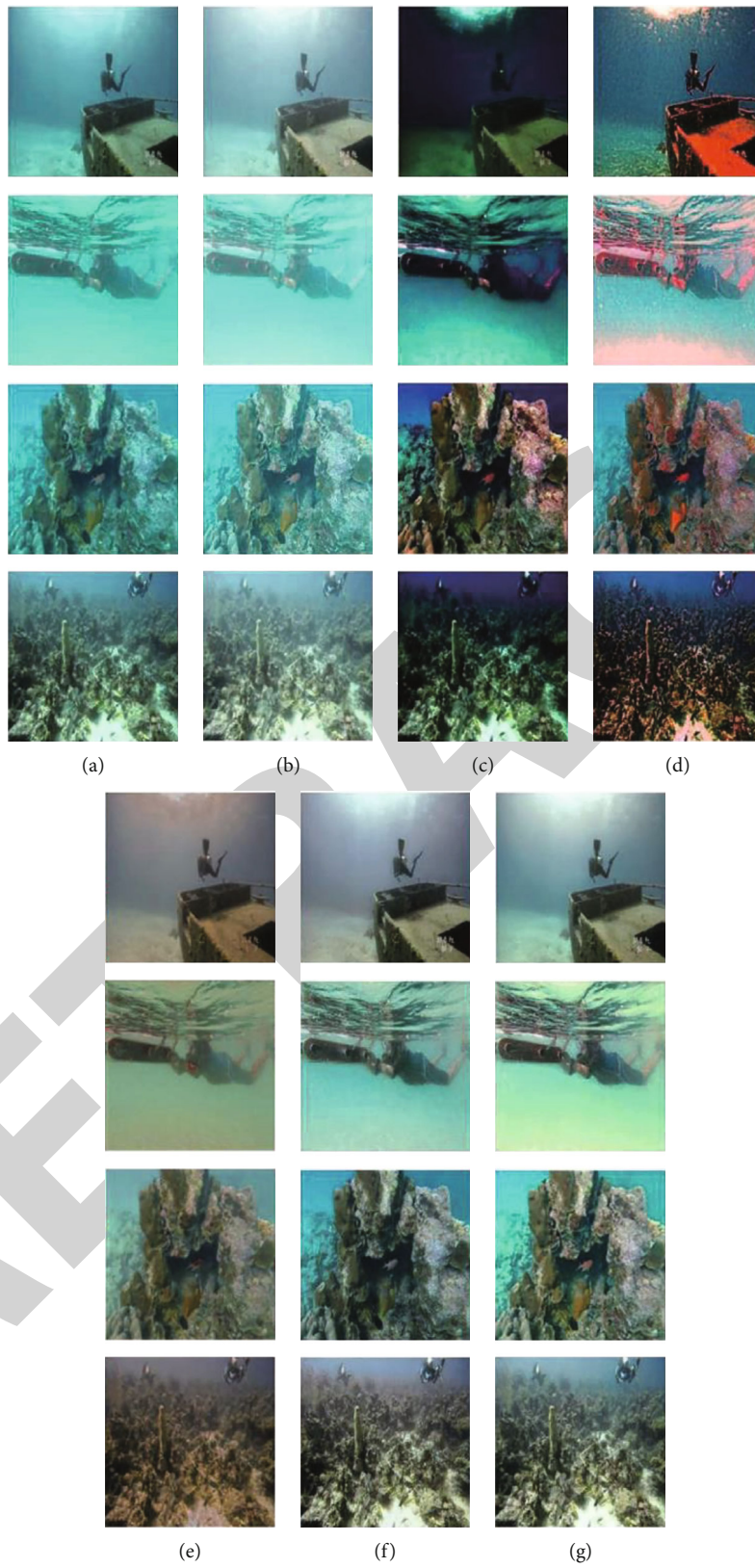
Figure 5: Qualitative comparison of different methods on test set B. (a) Underwater images; (b) GC; (c) UDCP; (d) LDCP; (e) UWCNN; (f) FUnIE-GAN; (g) proposed method.

Table 4: Quantitative comparison of different methods on test set B.

Metrics	GC	UDCP	LDCP	UWCNN	FUnIE-GAN	Ours
UIQM	2.33362	1.6765	2.0935	2.2209	2.3419	2.9457
IE	4.2287	4.4679	4.5453	3.3640	4.6503	4.6925
NIQE	28.6065	31.0209	27.7122	39.8557	41.1684	37.6926
OG-IQA	-0.4487	-0.6763	-0.7239	-0.5481	-0.7476	-0.8002

algorithms are compared qualitatively and quantitatively on test set A and test set B, respectively.

In order to demonstrate the effectiveness of the FPA module added to the generative network, a comparison between this model and the GAN model without the FPA module is performed. The two models are consistent in terms of the training set and the values of their hyperparameters. The results of the subjective experiments on the test set are shown in Figure 3.

As shown in Figure 3, the GAN model without the FPA module can effectively correct the underwater images with blue-green tones, but at the same time, it introduces yellowish color, and the overall image is dark, which has poor enhancement effect. In this paper, the algorithm dense features and contextual information of the image, which effectively improves the visual perception of the image, corrects the color bias, and enhances the contrast.

To further validate the effectiveness of the FPA module, the performance of the two models on test set A and test set B is quantitatively analyzed. First, two full-reference evaluation metrics, namely, PSNR and SSIM, were considered. Among them, the larger the PSNR and SSIM values are, the closer the brightness, contrast, overall structure, and information contained in the image to be evaluated are to the reference image. Secondly, three nonreference image quality evaluation metrics—UIQM, IE, and NIQE—were considered. The results of quantitative analysis are shown in Tables 1 and 2.

The experimental results in Table 1 show that after adding the FPA module, the distortion between the enhanced underwater image and the reference image is smaller, and the brightness, contrast, and structural information of the image are closer to that of the reference image.

The experimental results in Table 2 show that the enhanced underwater image performs better in the nonreference image quality evaluation index after adding the FPA module.

In order to verify the effectiveness of this algorithm, several experiments were conducted on test set A to compare this algorithm with existing underwater image enhancement methods (including GC, UDCP, LDCP, UWCNN, and FUnIE-GAN) qualitatively and quantitatively. The results of the qualitative comparison analysis of different methods on test set A are shown in Figure 4. It can be seen that the nonphysical model-based GC method does not enhance the image sufficiently, resulting in lighter color and fogging of the image. In contrast, the physical model-based methods (UDCP, LDCP) introduce unexpected colors, and the images show red or blue color bias. In turn, a lightweight convolutional neural network model

is designed to enhance the underwater images, which effectively removes fogging and improves clarity but introduces a yellowish color bias.

To further verify the performance of the algorithm in this paper, two full-reference image quality evaluation metrics, PSNR and SSIM, were used for quantitative comparison and analysis with the above methods. The results of quantitative analysis of different methods are shown in Table 3. From Table 3, we can see that the algorithm outperforms the other comparison algorithms in both PSNR and SSIM evaluation indexes, which indicates that the algorithm can effectively recover the information in the image, improve the contrast, and make the obtained image more realistic and natural.

In order to evaluate the performance of this algorithm more accurately, the qualitative and quantitative comparisons between this algorithm and the above underwater image enhancement methods were conducted on test set B. The qualitative comparison analysis of different methods on test set B is shown in Figure 5. As shown in Figure 5(b), although the GC method corrects the color deviation, it has not completely eliminated the blue-green hue of the underwater image and brings the fogging effect. From Figures 5(c) and 5(d), it can be seen that the physical model-based method for underwater images shows exposure and introduces red and blue color bias. As shown in Figure 5(e), the method in the literature [12] leaves room for improvement in terms of image brightness and haze removal. As shown in Figures 5(f) and 5(g), both the method in [17] and the algorithm in this paper perform better in terms of blue-green hue correction, sharpness enhancement, and visual perception of the image. However, the algorithm in this paper performs better in color correction, defogging, and visual perception, and the obtained images are clearer and more natural. Therefore, the algorithm in this paper has better generalization performance.

In order to objectively verify the performance of the algorithms in this paper, four nonreference image quality evaluation metrics, UIQM, IE, NIQE, and gradient correlation-based image quality assessment (OG-IQA), are selected to evaluate and compare the underwater images enhanced by the above methods. IE is an important indicator of the richness of information in an image, and the larger the value, the more informative the image is. OG-IQA uses the correlation between adjacent gradients to describe the degree of distortion of an image, and the smaller the value, the better the image quality. The average scores of different methods on each evaluation index are shown in Table 4.

Table 4 shows that, except for the NIQE evaluation index, the values of the other three evaluation indexes of this

algorithm are better than those of the comparison algorithm. For example, the UIQM evaluation index of this algorithm is higher than that of the comparison algorithm, with a value of 2.9457, which indicates that this algorithm can effectively improve the contrast and sharpness of the image and correct the color deviation. The values of IE and OG-IQA evaluation indexes are 4.6925 and -0.8002, respectively, which indicate that the enhanced images contain more information, less distortion, and higher visual quality.

6. Conclusion

This paper focuses on the low contrast and chromatic aberration of ocean underwater images and studies the specific methods of ocean underwater image enhancement. In this paper, neural network is used for enhancement. A bright color compensation and blending method is proposed. Underwater image enhancement algorithm uses GAN. Both qualitative analysis and quantitative analysis have achieved good results. Because the image color compensation based on the bright channel takes the average value of the bright channel as the estimation value of red, the marine landscape map not only has low contrast and color distortion but also has various degraded images due to changes in water turbidity and depth of field.

Data Availability

The experimental data used to support the findings of this study are available from the corresponding author upon request.

Conflicts of Interest

The authors declared that they have no conflicts of interest regarding this work.

Acknowledgments

References

[1] D. Wu, Y. Lei, M. He, C. Zhang, and L. Ji, "Deep reinforcement learning-based path control and optimization for unmanned ships," *Wireless Communications and Mobile Computing*, vol. 2022, Article ID 7135043, 8 pages, 2022.

[2] G. Cai, Y. Fang, J. Wen, S. Mumtaz, Y. Song, and V. Frascolla, "Multi-carrier M-ary DCSK system with code index modulation: an efficient solution for chaotic communications," *IEEE Journal of Selected Topics in Signal Processing*, vol. 13, no. 6, pp. 1375–1386, 2019.

[3] K. Chandra, A. S. Marcano, S. Mumtaz, R. V. Prasad, and H. L. Christiansen, "Unveiling capacity gains in ultradense networks: using mm-wave NOMA," *IEEE Vehicular Technology Magazine*, vol. 13, no. 2, pp. 75–83, 2018.

[4] X. Xie, X. Pan, W. Zhang, and J. An, "A context hierarchical integrated network for medical image segmentation," *Computers and Electrical Engineering*, vol. 101, article 108029, 2022.

[5] S. Palanisamy, B. Thangaraju, O. I. Khalaf, Y. Alotaibi, S. Alghamdi, and F. Alassery, "A novel approach of design and analysis of a hexagonal fractal antenna array (HFAA) for next-generation wireless communication," *Energies*, vol. 14, no. 19, p. 6204, 2021.

[6] S. N. Alsubari, S. N. Deshmukh, A. A. Alqarni et al., "Data analytics for the identification of fake reviews using supervised learning," *CMC-Computers, Materials & Continua*, vol. 70, no. 2, pp. 3189–3204, 2022.

[7] X. Xie, X. Pan, F. Shao, W. Zhang, and J. An, "Mci-net: multi-scale context integrated network for liver ct image segmentation," *Computers and Electrical Engineering*, vol. 101, article 108085, 2022.

[8] S. A. Bansode, V. R. More, S. P. Zambare, and M. Fahd, "Effect of constant temperature (20 0C, 25 0C, 30 0C, 35 0C, 40 0C) on the development of the Calliphorid fly of forensic importance, Chrysomya megacephala (Fabricus, 1794)," *Journal of Entomology and Zoology Studies*, vol. 4, no. 3, pp. 193–197, 2016.

[9] F. A. Al-Mekhlafi, R. A. Alajmi, Z. Almusawi et al., "A study of insect succession of forensic importance: dipteran flies (diptera) in two different habitats of small rodents in Riyadh City, Saudi Arabia," *Journal of King Saud University-Science*, vol. 32, no. 7, pp. 3111–3118, 2020.

[10] A. Algalil, M. A. Fahd, and S. P. Zambare, "New species of flesh fly (Diptera: Sarcophagidae) Sarcophaga (Liosarcophaga) geetai in India," *Journal of Entomology and Zoology Studies*, vol. 4, no. 3, pp. 314–318, 2016.

[11] A. M. Al-Azab, A. A. Zaituon, K. M. Al-Ghamdi, and F. M. A. Al-Galil, "Surveillance of dengue fever vector Aedes aegypti in different areas in Jeddah city Saudi Arabia," *Advances in Animal and Veterinary Sciences*, vol. 10, no. 2, pp. 348–353, 2021.

[12] A. R. Alqahtani, A. Badry, S. A. M. Amer, F. M. A. Al Galil, M. A. Ahmed, and Z. S. Amr, "Intraspecific molecular variation among Androctonus crassicauda (Olivier, 1807) populations collected from different regions in Saudi Arabia," *Journal of King Saud University-Science*, vol. 34, no. 4, article 101998, 2022.

[13] R. Ali, M. H. Siddiqi, and S. Lee, "Rough set-based approaches for discretization: a compact review," *Artificial Intelligence Review*, vol. 44, no. 2, pp. 235–263, 2015.

[14] P. E. Abas and L. C. De Silva, "Review of underwater image restoration algorithms," *IET Image Processing*, vol. 13, no. 10, pp. 1587–1596, 2019.

[15] X. Xie, W. Zhang, H. Wang et al., "Dynamic adaptive residual network for liver CT image segmentation," *Computers and Electrical Engineering*, vol. 91, article 107024, 2021.

[16] J. Lu, N. Li, S. Zhang, Z. Yu, H. Zheng, and B. Zheng, "Multi-scale adversarial network for underwater image restoration," *Optics & Laser Technology*, vol. 110, pp. 105–113, 2019.

[17] M. J. Islam, Y. Xia, and J. Sattar, "Fast underwater image enhancement for improved visual perception," *IEEE Robotics and Automation Letters*, vol. 5, no. 2, pp. 3227–3234, 2020.

[18] S. Lin, K. Chi, T. Wei, and Z. Tao, "Underwater image sharpening based on structure restoration and texture enhancement," *Applied Optics*, vol. 60, no. 15, pp. 4443–4454, 2021.

[19] M. Wenjuan and X. Feng, "Retracted article: underwater image segmentation based on computer vision and research on

recognition algorithm," *Arabian Journal of Geosciences*, vol. 14, no. 18, pp. 1–11, 2021.

[20] R. Chen, Z. Cai, and W. Cao, "MFFN: an underwater sensing scene image enhancement method based on multiscale feature fusion network," *IEEE Transactions on Geoscience and Remote Sensing*, vol. 60, pp. 1–12, 2021.

[21] Y. Li and R. Chen, "SE–RWNN: an synergistic evolution and randomly wired neural network-based model for adaptive underwater image enhancement," *IET Image Processing*, vol. 14, no. 16, pp. 4349–4358, 2020.

[22] M. Mathur and N. Goel, "Enhancement algorithm for high visibility of underwater images," *IET Image Processing*, vol. 16, no. 4, pp. 1067–1082, 2022.

[23] S. Raveendran, M. D. Patil, and G. K. Birajdar, "Underwater image enhancement: a comprehensive review, recent trends, challenges and applications," *Artificial Intelligence Review*, vol. 54, no. 7, pp. 5413–5467, 2021.

[24] L. Chen, Z. Jiang, L. Tong et al., "Perceptual underwater image enhancement with deep learning and physical priors," *IEEE Transactions on Circuits and Systems for Video Technology*, vol. 31, no. 8, pp. 3078–3092, 2021.

[25] T. Li, S. Rong, W. Zhao et al., "Underwater image enhancement using adaptive color restoration and dehazing," *Optics Express*, vol. 30, no. 4, pp. 6216–6235, 2022.